IOP Publishing
Journal of Physics: Condensed Matter
J. Phys.: Condens. Matter **30** (2018) 204004 (11pp)
https://doi.org/10.1088/1361-648X/aab99a

Smectic viral capsids and the aneurysm instability

S Dharmavaram[1], **J Rudnick**[1], **C M Lawrence**[2,3] **and R F Bruinsma**[1,4,5]

[1] Department of Physics and Astronomy, University of California, Los Angeles, CA 90095, United States of America
[2] Thermal Biology Institute, Montana State University, Bozeman, MT 59717, United States of America
[3] Department of Chemistry and Biochemistry, Montana State University, Bozeman, MT 59717, United States of America
[4] Department of Chemistry and Biochemistry, University of California, Los Angeles, CA 90095, United States of America

E-mail: bruinsma@physics.ucla.edu

Received 22 December 2017, revised 13 March 2018
Accepted for publication 26 March 2018
Published 26 April 2018

Abstract

The capsids of certain *Archaea*-infecting viruses undergo large shape changes, while maintaining their integrity against rupture by osmotic pressure. We propose that these capsids are in a *smectic liquid crystalline state*, with the capsid proteins assembling along spirals. We show that smectic capsids are intrinsically stabilized against the formation of localized bulges with non-zero Gauss curvature while still allowing for large-scale cooperative shape transformation that involves global changes in the Gauss curvature.

Keywords: smectic liquid crystal, capsids of archaeal viruses, aneurysm instability

(Some figures may appear in colour only in the online journal)

1. Introduction

Viruses package their genetic material (DNA or RNA) inside a protein shell: the capsid. Capsids have remarkable materials properties. Some can withstand internal osmotic pressures as high as tens of atmospheres [1] and large mechanical deformations without rupture [2] while others are able to function in extreme physical environments such as high salinity, acidity and temperature [3]. These features make viral capsids of interest for materials science applications (in particular when combined with the intrinsic programmability of viruses [4]). The structural basis of viral capsids that makes them so robust is normally assumed to derive from the fact that capsid proteins self-assemble into shells composed of an interlocked array of proteins. These positionally-ordered capsids are most frequently either cylindrically shaped helical assemblies or spherically shaped icosahedral structures, where the symmetry of the icosahedral capsids are classified according to their triangulation numbers as described by Caspar and Klug (CK) [5].

Forty years ago molecular phylogenetics recognized Archaea as a separate domain or kingdom of life [6]. In conjunction with bacteria and the nucleated eukaryotes, this resulted in three major branches, or domains in the universal tree of life; the Archaea, the Bacteria and the Eucarya [7]. While Archaea are like bacteria in size and shape, their transcriptional and translational machinery is closer to that of plant and animal cells (eukaryotes), and they may utilize metabolic pathways such as methanogenesis that are unique to certain archaea (methanogens). Further, while Archaea are abundant in soils, oceans and the mammalian GI tract, they are also the dominant organisms in extreme habitats, with halophiles found in hypersaline lakes, acidophiles that thrive in highly acidic springs and acid mine drainage, alkaliphiles in basic environments, and hyperthemophiles that thrive at or near the boiling point of water. For those living at high temperatures, the membrane lipids and membranes are also unlike those of either bacteria or eukaryotes [8].

Like Eucarya and Bacteria, the Archaea are also subject to infection by viruses. The study of archaeal viruses is a young field and fewer than 100 viruses have been studied in any detail

---

[5] Author to whom any correspondence should be addressed.

© 2018 IOP Publishing Ltd Printed in the UK

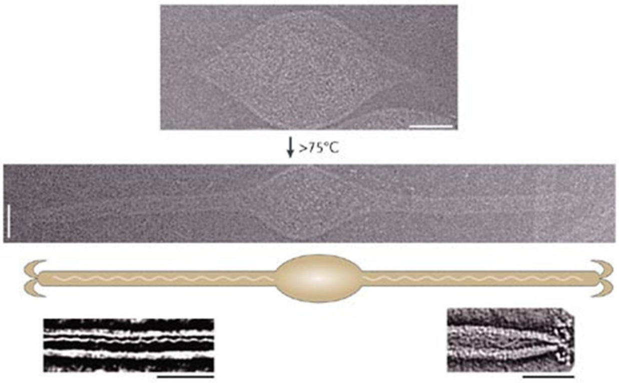

Figure 1. Cryo-electron micrographs of the conformational change of ATV and its reconstruction. Reprinted by permission from Macmillan Publishers Ltd: Nature Reviews Microbiology [14], Copyright 2006.

[3]. However, this work has already given rise to 17 new viral families [3]. For historical reasons, these viruses are largely associated with either the thermophilic crenarchaeota or the halophilic euryarchaeota, although viruses infecting additional phyla are abundant and begging for attention [9]. Initial studies suggested euryarchaeal viruses are typical head-and-tail phages, though recent studies suggest this is an oversimplification [10]. In contrast, viruses infecting Crenarchaea frequently exhibit remarkably unusual and diverse morphotypes, rather than the more common icosahedral or cylindrically shaped morphologies [3, 11]. In particular, three viral families (Fuselloviridae, Bicaudaviridae, Salterprovirus) are characterized by spindle-shaped (lemon-shaped) capsids [3, 12]. In terms of physical virology this presents us with a fundamental challenge: these capsids cannot be a positionally-ordered protein shells because the spindle shape necessitates the introduction of a large number of five-fold and seven-fold topological defects [13].

One of the best examples of spindle-shaped capsid morphology is Acidianus two-tailed virus (ATV) [14, 15] shown in figure 1. As it exits an infected cell, the ATV capsid initially appears as a tailless lemon-shaped particle. However, over time it grows extended, cylindrical tails at each end of the central, spindle-shaped capsid [14]. This shape change may be driven by the polymerization of a central protein filament that runs the length of the capsid. The two protruding tails are believed to play a role in establishing contact with potential host cells [14], as is the case with more typical bacterial viruses (phage). Importantly, as the tails elongate over time, the volume of the capsid decreases to approximately half its initial volume, yet the overall surface area of the particle remains roughly constant [14]. This suggests the major structural protein(s) in the tails are the same as those in the lemon-shaped capsid. Further, this morphological change occurs at 75 °C and above; tailless lemon-shaped ATV stored at lower temperatures do not show this morphological transition.

It is well known that the deformation of a positionally-ordered layer of particles which involves a change in the Gauss curvature of the layer requires the introduction of topological defects in the particle array including disclinations, dislocations, and strings of dislocations [16]. In a previous publication [13], we investigated the possibility that these lemon-shaped archaeal capsids have an intrinsic distribution of *mobile* topological defects. A layer of material with mobile topological defects would be solid-like on short time scales and liquid-like on long time scales, i.e. it would be *visco-elastic* [17].

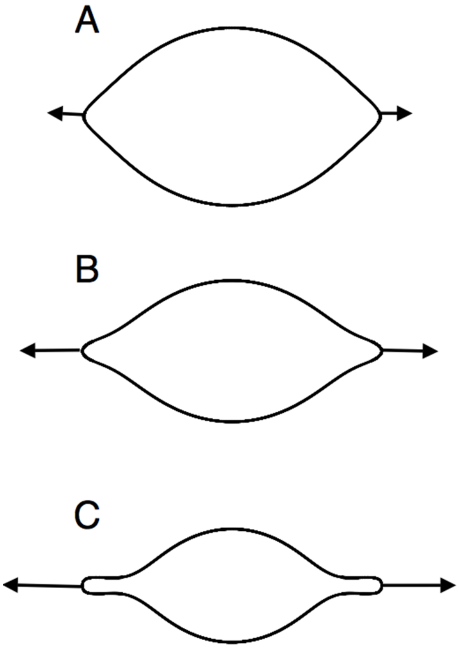

Figure 2. Simulation of the shape of a tense shell in the liquid state with a non-zero bending energy that is progressively stretched between two points on opposite sides of the shell. Pulling force increases from top to bottom. Note the reduction in volume. The surface area was kept fixed.

Figure 2 shows the results of a simulation of the effects of pulling out two points located on opposite sides of a shell in the liquid state that is stretched due to a pressure difference between the interior and exterior. The shell has non-zero surface bending modulus κ and a fixed surface area $A = 4\pi R^2$. The enclosed volume was not fixed however. The pulling force represents the force exerted by the polymerization of the central filament [18]. At a critical point (close to B), two tethers are suddenly pulled out. The radius of the two tethers depends on the bending modulus. The reason for the sudden appearance of the tethers is explained in figure 3 and [19].

Figure 2 compares rather well with figure 1 for the shape change of the ATV capsid. This would support the notion that the ATV capsid is in a liquid state. It is easy to obtain an approximate analytical expression for the shape of the shell. The contribution from the bending energy is important only in the regions of the shell that are connected to the tethers. If we can neglect the bending energy then the free energy of a stretched fluid shell with volume V, surface area S, and maximum spanning distance L expressed as $F_l = -\Pi V + \gamma S - \tau L$ with Π the pressure difference between the interior and exterior, γ the surface tension, and τ the stretching force. When this expression is minimized with respect to the shape of the shell, one finds that the condition of mechanical equilibrium imposes the *Laplace Law* $\Pi = 2\gamma H$, with H the mean curvature of the shell. It follows that the equilibrium shape of a liquid shell enclosing a volume with uniform pressure has

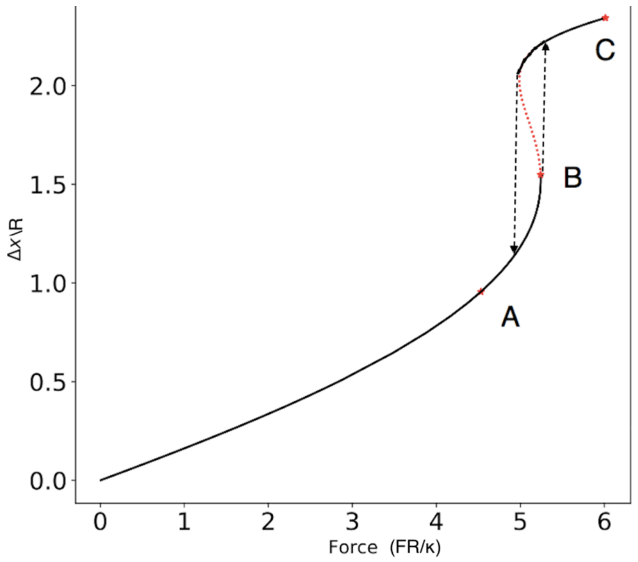

Figure 3. Force-extension curve for the shell of figure 2. Vertical axis: distance Δx is the between the two pulling points minus diameter $2R$ of the undeformed shell, where $4\pi R^2$ is the fixed surface area measured in units of R. Horizontal axis: pulling force in units of the bending modulus κ divided by R. The points marked A, B, and C correspond to the three shapes of figure 2. A mechanically unstable section is indicated by a dashed red line. Dashed black arrows indicate a hysteresis loop. For a typical spindle shaped virus [20] $R = 100\,\mathrm{nm}$, $\Pi = 10$ atm, radius of tail is $r = 4\,\mathrm{nm}$ from which we estimate $\kappa = r^2\Pi R \approx 400 k_B T$ [19]. For this choice, the unit of force is 16 pN and the unit of displacement is 100 nm.

to be that of a *surface of constant mean curvature*. The only surface of constant mean curvature that resembles the ATV capsid is the *unduloid*, a surface of revolution generated by the rotation of a catenary around an axis [21]. The central part of the computed shell shape indeed agrees reasonably with that of an unduloid.

We performed in [13] a finite temperature Monte-Carlo simulation of interacting particles located on the surface of an unduloid. The simulation revealed (i) that the negative Gauss curvature of an unduloid covered by a particle array automatically generates a plethora of dislocations, disclinations, and strings of dislocations and (ii) that these topological defects remain mobile at temperatures well below the nominal melting temperature of the particle array. The same numerical simulations revealed however that isotropic viscoelastic shells may have serious defects in terms of their function as capsids. Unlike a positionally ordered layer of particles, a viscoelastic layer may not be able to resist the formation of bulges. In the simulations, we observed significant variations in the local tension around the structural defects. As will be discussed in more detail later, variations in the tension across the surface of a pressure vessel can lead to the growth of bulges, as happens during the formation of aneurysms on blood vessels. In this context, it should be noted that it is not known if the osmotic pressure inside ATV capsids is as high as that of bacterial viruses (phage) [1], although an internal pressure of 10 ATM has been shown for His1, a salterprovirus with a lemon-shaped capsid [22].

Recently, crystallographic and cryo-EM studies of Acidianus tailed spindle-shaped virus (ATSV), a second member of the large tailed spindle virus superfamily, suggest that the major coat protein assembles as a multistart helix that runs through the tail and then extends into the spindle-shaped capsid [20]. Importantly, the side-by-side or intrastrand interactions between capsid protein subunits within a helix or spiral appear significantly stronger than the inter-strand interactions between spirals. In this paper it is proposed that the capsids of ATV and ATSV are *anisotropic* visco-elastic materials, specifically *smectic liquid crystals*, driven by the polymerization of capsid proteins into spirals. In section 2 we present a model free energy for capsids in the smectic state, based on a chiral version of the Landau–Brazovskii Hamiltonian. In section 3, we show an ATV-like capsid in the smectic state can undergo large-scale shape changes without a prohibitive energy penalty while in section 4 we examine the resistance of such vesicles against bulge formation.

2. Chiral smectics on a curved surface

2.1. Free energy of a chiral smectic capsid

The free energy of a capsid in the smectic liquid crystal state will be assumed to be the sum of the free energy F_l of the capsid in the liquid state, as discussed in section 1, plus a contribution ΔF associated with the formation of chiral smectic order. The latter is given by

$$\Delta F_{sm} = \frac{1}{2}\int \mathrm{d}a \left(\left|(\Delta + k_0^2)\Psi\right|^2 + r|\Psi|^2 + u|\Psi|^4 \right) + \chi \int \mathrm{d}a \nabla\Psi \cdot \mathbf{C} \cdot (\nabla\Psi^* \times \hat{\mathbf{n}}). \tag{2.1}$$

The first part of ΔF, which we will denote by F_{LB}, is the *Landau–Brazovskii Hamiltonian* (LB) for a complex order parameter $\Psi = A\exp\mathrm{i}\phi$ with amplitude A and phase function ϕ. The coefficient of the term $\left|(\Delta + k_0^2)\Psi\right|^2$ was set equal to one by choosing suitable units for the order parameter amplitude. As a consequence, A^2 has dimensions of energy times area. To see the connection between smectics and the LB Hamiltonian, it is useful to express the order parameter in terms of the phase and amplitude variables:

$$F_{\mathrm{LB}} = \frac{1}{2}\int \mathrm{d}a \Big(\left[A(k_0^2 - |\nabla\phi|^2) + \Delta A\right]^2 + \left[A\Delta\phi + 2\nabla A \cdot \nabla\phi\right]^2 + \left[rA^2 + uA^4\right] \Big). \tag{2.2}$$

For negative r and positive u and for a flat surface, F_{LB} is minimized by a density wave of the form $\Psi_0(\vec{r}) = A_0\exp(\mathrm{i}k_0\hat{\mathbf{n}}.\vec{r})$ with wavevector $k_0\hat{\mathbf{n}}$ and amplitude $A_0 = \sqrt{-r/2u}$ where $\hat{\mathbf{n}}$ is an arbitrary unit vector in the plane. The real part of $\Psi_0(\vec{r})$ can be viewed as a smectic density modulation with amplitude A_0. Since A_0 goes to zero at $r = 0$, this point would mark the (mean-field) onset of smectic ordering.

If the amplitude is assumed constant while the phase is allowed to vary at will, then F_{LB} reduces to

$$F_{\mathrm{LB}} = \frac{1}{2}A_0^2 \int \mathrm{d}a \Big(\left[k_0^2 - |\nabla\phi|^2\right]^2 + (\Delta\phi)^2 \Big) \tag{2.3}$$

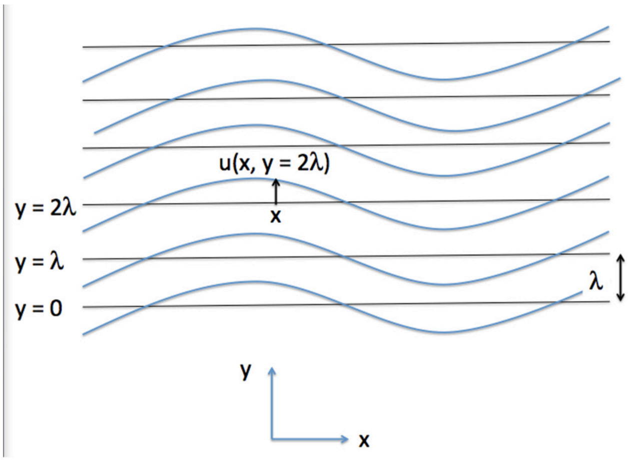

Figure 4. Crests of a deformed density wave. The undeformed density wave is directed along the y-direction and has a wavelength λ. The maxima of the wave are lines along the x-direction with $y = \mathrm{i}\lambda$, where $i = 0, 1, 2, 3, ..$ is an integer. In the deformed state, the maxima are displaced by $u(x, y)$ along the y-direction.

where we dropped a constant term that can be absorbed into F_l. As shown in figure 4, a phase function $\phi(x, y) = k_0(y - u(x, y))$ describes a deformed density wave along the y-direction with the smectic stripes displaced over a distance $u(x, y)$ along the y-direction.

The LB free energy expressed in terms of $u(x, y)$ is

$$F_{\mathrm{LB}} = \frac{1}{2}\int \mathrm{d}a\Big(B\Big[\partial u/\partial y + \frac{1}{2}(\nabla u)^2\Big]^2 + K(\Delta u)^2\Big). \tag{2.4}$$

This is the Grinstein–Pelcovits (PE) expression for the deformation energy of a 2D smectic liquid crystal [23]. It is the sum of a stripe compression energy and a stripe bending energy term. The compression modulus is $B = 4A_0^2k_0^4$ and the stripe bending modulus is $K = A_0^2k_0^2$. Note that both moduli go to zero at the onset of smectic ordering.

Yet another way to write F_{LB} is to express the phase gradient as $\nabla\phi = k_0\hat{\mathbf{n}}(\vec{r})$ where $\hat{\mathbf{n}}(\vec{r})$ now is a position-dependent unit vector normal to the lines of constant phase:

$$F_{\mathrm{LB}} = \frac{1}{2}\int \mathrm{d}a\Big((1/4)B\left[1 - (|\nabla\phi|/k_0)^2\right]^2 + K(\nabla.\hat{\mathbf{n}})^2\Big). \tag{2.5}$$

The divergence $\nabla.\hat{\mathbf{n}}$, which is similar to the splay term for nematic liquid crystals, represents the energy cost of bending the lines of constant phase. This version is useful when considering smectics on curved surfaces. The first term of equation (2.5) is minimized by $|\nabla\phi| = k_0$. For a curved surface, this equation has the mathematical form of the *eikonal equation* for the rays of geometrical optics, as noted in [24]. The smectic stripes behave here like the wavefronts of a monochromatic wave that travels along the curved surface according to geometrical optics. This term is minimized if the smectic stripes are *geodesics* of the curved surface, i.e. lines of shortest distance between two points measured along the surface. For a curved surface, the term $(\Delta\phi)^2$ introduces coupling between the smectic order parameter and the Gauss curvature of the surface. Note that the Δ operator is to be interpreted as the Laplace–Beltrami operator on curved surfaces, which only is affected by the Gauss curvature of a surface.

The LB Hamiltonian is not the most general free energy for a 2D smectic because it does not include coupling between the mean or extrinsic curvature H of the surface and the order parameter Ψ. This is not a very serious concern in the present context because our focus is on the resistance against bulge formation, which is due to coupling between the Gauss or intrinsic curvature and the smectic order parameter[6], as will be discussed further in section 3.

The second term of equation (2.1) will be denoted by F_{HP}. Since capsid proteins are *chiral*, capsids should be represented as chiral surfaces. F_{HP} is the Helfrich–Prost (HP) free energy for chiral layers [26]:

$$F_{\mathrm{HP}} = \chi\int \mathrm{d}a\,[\nabla\Psi\cdot\mathbf{C}\cdot(\nabla\Psi^*\times\hat{\boldsymbol{\rho}})]. \tag{2.6}$$

The two-by-two matrix $\mathbf{C}$ is the curvature tensor of the surface and $\hat{\boldsymbol{\rho}}$ is the outward normal unit vector to the surface. Note that the integrand is a *pseudo-scalar*, i.e. it is odd under inversion. If one takes the amplitude A again to be a constant then the HP term simplifies to

$$F_{\mathrm{HP}} = \chi K\int \mathrm{d}a\,[\hat{\mathbf{n}}\cdot\mathbf{C}\cdot\hat{\mathbf{t}}] \tag{2.7}$$

where $\hat{\mathbf{t}} = \hat{\mathbf{n}}\times\hat{\boldsymbol{\rho}}$ is a unit vector tangent to the stripes. The strength χ of the chirality has, in our units, dimensions of an inverse length.

As an example of how the HP term works, consider a cylindrical surface of radius a. The minimum energy state of the LB Hamiltonian is one where the smectic stripes form a collection of equidistant spirals separated by the wavelength $\lambda = 2\pi/k_0$ of the density wave. If there are M separate spirals on the cylinder then the pitch angle ψ of the stripes with respect to the cylinder axis is geometrically related to the number M of spirals by $M = (k_0a)\sin\psi$. We can now evaluate the HP term. The curvature tensor $\mathbf{C}$ of a cylinder in polar coordinates has only a single nonzero entry, equal to $1/a$. It follows that the HP term equals $-\chi(k_0A_0)^2(1/a)\sin 2\psi$ per unit area. This is minimized by setting $\psi = \pm\pi/4$, depending on the sign of the ξ. The number of independent spirals is then $M = (k_0a)/\sqrt{2}$. Because a cylinder has zero Gauss curvature, the LB Hamiltonian does not contribute to the determination of the pitch angle of the spiraling smectic stripes on a cylinder.

3. Smectic unduloids

Recall that the capsid has the shape of an unduloid if the smectic order parameter is zero. A logical step is thus the computation of ΔF_{sm} for an unduloid surface. We will assume an unduloid with smallest diameter $2a$ and largest diameter $2c$, as shown in figure 5. In this limit, The constant mean curvature equals $H = 1/(a + c)$ so the Laplace Law takes the form

---

[6] The LB Hamiltonian version was applied earlier in [25] to describe layers of diblock copolymers on curved surfaces.

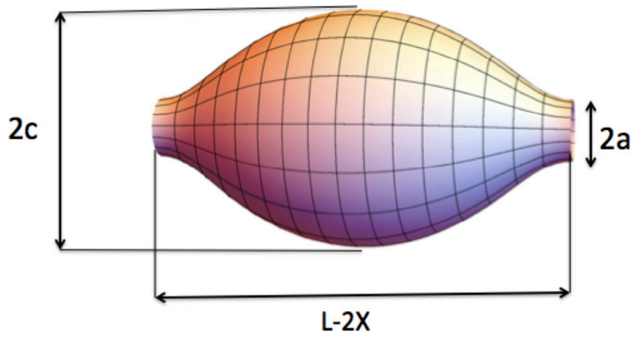

Figure 5. Unduloid. The smallest diameter is $2a$, the largest diameter is $2c$. The ATV shell corresponds to the limit $a \ll c$.

$\Pi = 2\gamma/(a+c)$. We will assume that the unduloid is matched to cylindrical tails with fixed diameter $2a$ so the ratio c/a is the only free parameter that determines the shape.

Introduce a polar coordinate system with the z-axis along the center-line of the unduloid. The unduloid surface can be defined in terms of the parametric curvilinear coordinates u and φ through

$$\mathbf{r}(u,\varphi) = [\rho(u)\cos\varphi, \rho(u)\sin\varphi, z(u)]$$
$$u \in [0, 2\pi],\ \varphi \in [0, 2\pi] \tag{3.1}$$

where,

$$z(u) = aF(\frac{u}{2} - \frac{\pi}{2}|k^2) + cE(\frac{u}{2} - \frac{\pi}{2}|k^2),$$

and where

$$\rho(u) = \sqrt{n - m\cos u}.$$

Here, F and E are incomplete elliptic integrals with modulus $k^2 = (c^2 - a^2)/c^2$. Next, $m = (c^2 - a^2)/2$ and $n = (c^2 + a^2)/2$.

In these coordinates, the eikonal equation $|\nabla\phi|^2 = k_0^2$ takes the form

$$\frac{4}{(a+c)^2}\phi_u^2 + \frac{1}{\rho^2}\phi_\varphi^2 - k_0^2 = 0. \tag{3.2}$$

Look for a solution with separation of variables $\phi(u,\varphi) = f(u) + M\varphi$ where M is the number of separate smectic stripes covering the unduloid. The eikonal equation reduces to

$$\frac{4f_u^2}{(a+c)^2} + \frac{M^2}{\rho^2} - k_0^2 = 0 \tag{3.3}$$

or

$$f_u^2 = (a+c)^2\frac{(k_0^2\rho(u)^2 - M^2)}{4\rho(u)^2}. \tag{3.4}$$

Using this equation, $f(u)$ can be expressed in the form of integral for given $\rho(u)$. It can be shown that equation (3.4) for the lines of constant phase of the eikonal solution defines a set of M equidistant (or Archimedean) spirals. An example is shown in figure 6 for $M = 8$.

To obtain an idea of the positioning of capsid proteins in the smectic state on an unduloid surface, we can populate these concentric spirals with small spheres representing the capsid proteins (see also [13]). Figure 7—borrowed from [13]—shows the result of the application of the Voronoi construction to the particle positions.

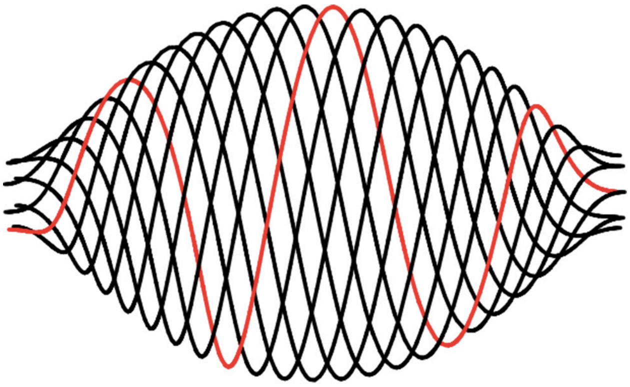

Figure 6. Solution of the eikonal equation on an unduloid covered by $M = 8$ with an initial pitch angle $\psi = \pi/2$. Shown are lines of constant phase. One of them is highlighted in red for clarity. Reprinted figure with permission from [13], Copyright 2016 by the American Physical Society.

One can identify dislocations in the form of pentamer–heptamer pairs and grain boundaries in the form of strings of pentamer–heptamer pairs. Note that that the grain boundaries emerge from the two necks in the form of spirals. The spirals can have either chirality, with only one of the two isomers shown in figure 7. If the HP term would be included, then this chiral degeneracy would be broken. Note that for this state to represent a visco-elastic smectic, thermal fluctuations need to be sufficiently strong to allow the protein spirals to slide past each other.

3.1. Cooperative shape changes

We now can compute $\Delta F_{sm} = F_{\mathrm{LB}} + F_{\mathrm{HP}}$ for a chiral smectic unduloid. We start with F_{LB}.

Assuming the eikonal solution, F_{LB} reduces for an unduloid to a pure bending energy $F_b = \frac{1}{2}K\int \mathrm{d}a\,[\nabla\cdot\hat{\mathbf{n}}_e]^2$ (the subscript e indicates the eikonal state). The bending energy has the scaling form $F_b/K = g_b(a/c)$, where $g_b(x)$ is a dimensionless scaling function that can be determined numerically once the initial slope $f_u(u=0)$ for the eikonal equation and the number M of independent spirals are specified. To that purpose, we will impose the requirement that the smectic state on the unduloid is matched, at $u = 0$ and $u = 2\pi$, to two cylindrical smectic surfaces with radius a that representat the tails. The unduloid and cylindrical surfaces must have the same number M of spirals. This number M is geometrically related to the pitch angle ψ of the spirals by $M = (k_0 a)\sin\psi$, which has to be valid in particular at the matching points. It then follows from equation (3.4) that $f_u(0) = \frac{1}{2}k_0(a+c)\sin\psi$. The only remaining free parameter is the pitch angle ψ for the spirals. The pitch angle must be determined by minimizing the total free energy (i.e. the sum ΔF of the chiral energies of the cylinders and the unduloid plus the bending energy of the unduloid (the bending energy of the cylinders is zero).

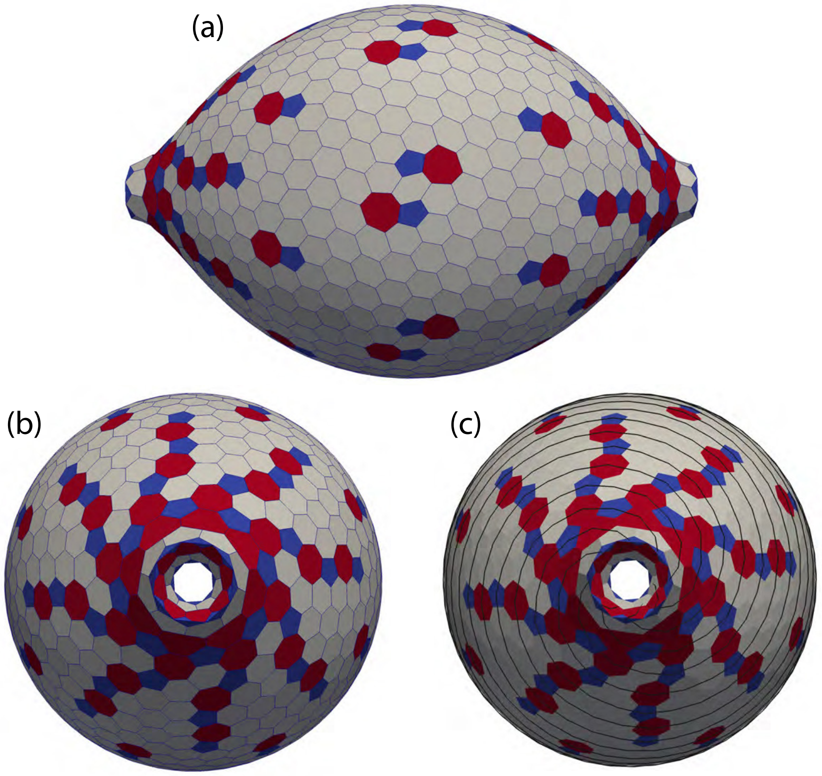

Figure 7. Voronoi construction for an array of spherical particles that populate the eight equidistant spirals of figure 6. Cells with five edges are colored blue (pentamers), cells with six edges grey (hexamers), and cells with seven edges red (heptamers). (a) Side view showing isolated dislocations; (b) Front view showing eight spiral dislocations strings; (c) Front view overlaid with spirals. Reprinted figure with permission from [13], Copyright 2016 by the American Physical Society.

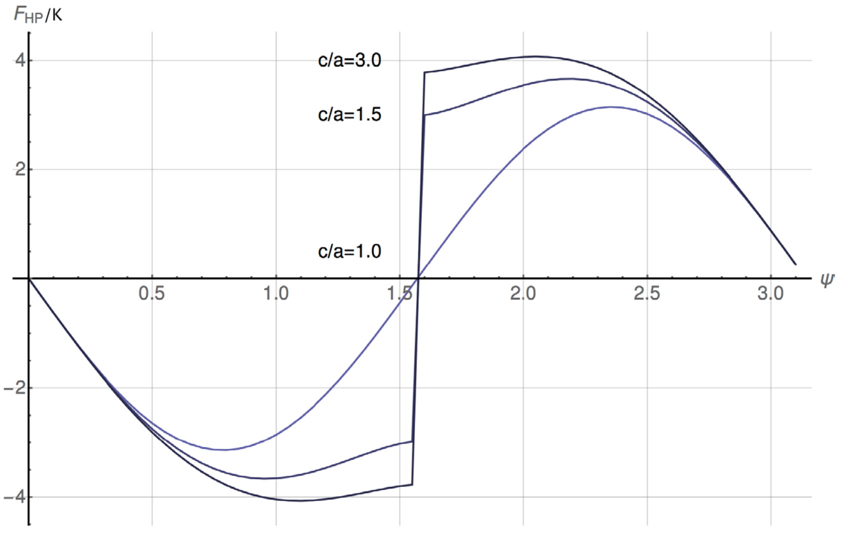

Figure 8. Chiral energy F_{HP}/K as a function of the initial pitch ψ for different values of *c*/*a*. The dimensionless strength $\chi(a/K)$ of the chiral interaction was equal to $1/2\pi$.

The chiral energy $F_{\mathrm{HP}}(\psi)$ of the unduloid can be shown to have the form

$$F_{\mathrm{HP}}(\psi) = \mp\left(2\pi\chi a^2 c\sin\psi\right) \times \int_0^{2\pi} \frac{\sqrt{\rho(u)^2 - a^2\sin^2\psi}}{\rho(u)^3}\,\mathrm{d}u. \quad (3.5)$$

In figure 8 we plot $F_{\mathrm{HP}}(\psi)$ as a function of ψ. For $c/a = 1$, the unduloid reduces to a cylinder when the chiral energy is proportional to $\sin 2\psi$ with a minimum at $\pi/4$ for positive χ (or $-\pi/4$ for negative χ). If *c*/*a* is larger than one then the minimum of F_{HP} is between $\pi/4$ and $\pi/2$, approaching $\pi/2$ for large *c*/*a*. F_{HP} has a discontinuity at $\psi = \pi/2$. Both spiral states at $\psi = \pi/2$ circle around the necks of the unduloid but with opposite chirality while the pitch angle is either larger or smaller than $\pi/2$. The chiral energies of these two states have opposite sign. For positive χ, the optimal pitch angle of the unduloid lies between $\pi/2$ and $\pi/4$.

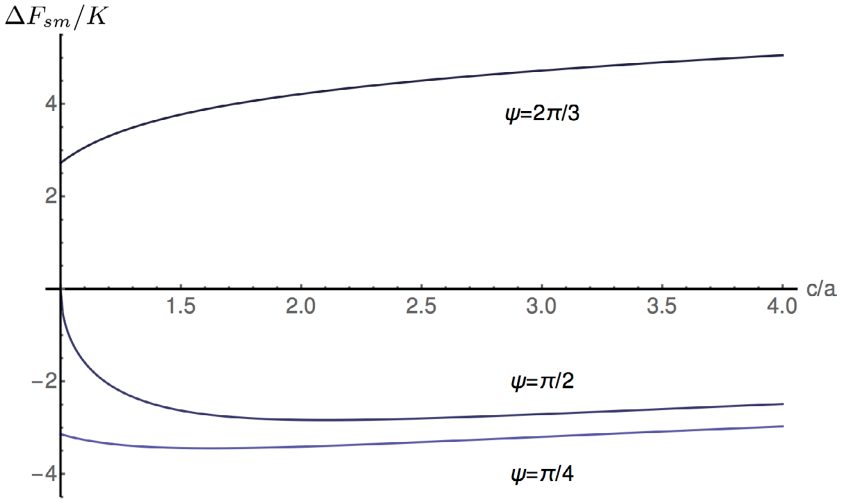

Figure 9. Smectic free energy $\Delta F_{sm}/K$ as a function of c/a for different values of the pitch-angle ψ. The dimensionless strength $\chi(a/K)$ of the chiral interaction was equal to $1/2\pi$ as in the previous figure.

We can now compute the sum ΔF_{sm} of the chiral and bending energies of the unduloid as a function of the ratio c/a. The result is shown in figure 9 for different values of the initial pitch angle ψ. The value of the pitch angle is determined by minimization of the *total* free energy (i.e. unduloid plus tails). First consider the case that the cylindrical tails are so long that their surface area is large compared to that of the unduloid. The minimization of the total energy is then dominated by the tails, which imposes the value $\psi = \pi/4$ for positive χ. The plot of ΔF_{sm} for $\psi = \pi/4$ shows that it is a smoothly varying function of c/a. In the opposite case of very short tails, it is the unduloid that determines the value of ψ. Now, the optimal value for ψ is between $\pi/2$ and $\pi/4$ depending on the c/a ratio (see figure 8). For large c/a the optimal pitch angle is $\pi/2$. In that regime, ΔF_{sm} remains a smoothly function of c/a. As c/a is reduced, the optimal pitch angle slowly shifts from $\pi/2$ to $\pi/4$. In that regime ΔF_{sm} again is only weakly dependent on c/a.

In summary, the smectic free energy ΔF_{sm} is a (very) smooth function of c/a. We can conclude that an unduloid-shaped capsid in the smectic state can undergo a large cooperative shape change that does involve a change in Gauss curvature without incurring a large free energy penalty.

3.2. Validity of the eikonal solution

The eikonal solution is *not* the minimum free energy state and the conclusion of the last subsection could be questioned on that basis. To investigate deviations from the eikonal solution, perform a perturbation expansion $\phi = \phi_e + \delta\phi$ where ϕ_e is the solution of the eikonal equation (with $\nabla\phi_e = k_0\hat{\mathbf{n}}_e$) (note that it is *a priori* not clear what the small expansion parameter is of this perturbation theory).

Leaving out for now the chiral term, the change in free energy δF produced by $\delta\phi$ is

$$\delta F = \int \mathrm{d}aA_0^2\Big(k_0\,[\nabla\cdot\hat{\mathbf{n}}]\,\Delta\delta\phi + 2k_0^2\,[\hat{\mathbf{n}}\cdot\nabla\delta\phi]^2 + \frac{1}{2}(\Delta\delta\phi)^2\Big). \tag{3.6}$$

There is one first-order term in $\delta\phi$ and two second-order terms. Let R be the local scale of variation of the eikonal solution ϕ_e, which is of the order of c except near the ends of the unduloid where it is of the order of a. We will assume R to be large compared to the'microscopic' length scale $2\pi/k_0$ of the problem, which is the case if $M \gg 1$. The first-order term in δF then scales as $(k_0/R^3)\delta\phi$, while the two second-order terms scale as $(k_0^2/R^2)\delta\phi^2$, respectively, $(1/R^4)\delta\phi^2$. Since $k_0R \gg 1$, we need retain only the first of the two second order terms. The Euler–Lagrange equation for the minimization of the sum of the first order term and the first second order term has the formal solution $\hat{\mathbf{n}}_e\cdot\nabla\delta\phi = (1/4k_0)(\hat{\mathbf{n}}_e\cdot\nabla)^{-1}\Delta\nabla\cdot\hat{\mathbf{n}}_e$. Power-counting shows that $\delta\phi$ is of the order of $\delta\phi \sim 1/(k_0R)$. We can neglect this term under the stated assumption that $k_0R \gg 1$.

A similar calculation shows that the expansion parameter associated with the chiral term is χ/k_0. That is, the characteristic length scale introduced by chirality should be large compared to the microscopic length. In short, the eikonal solution remains valid provided the wavelength $2\pi/k_0$ is small compared to all other length-scales of the problem (here, a, c, and $1/\chi$).

4. Bulge formation

We found that the free energy of a smectic unduloid is a smooth function of the aspect ratio of the unduloid, which means that smectic ordering does not suppress global shape changes. We now turn to the question whether smectic ordering can suppress aneurysm-type instabilities. We first briefly review the physics of bulge formation for a tense liquid shell under pressure.

Assume a uniform spherical solid shell of radius R with a pressure difference P between the interior and exterior of the shell. The tension γ_0 in the shell is related to the pressure difference P between the interior and exterior by the Laplace Law $P = 2\gamma_0/R$ for mechanical equilibrium. Now assume that the elastic properties of the shell are not uniform, so the wall tension depends on position. The Laplace Law for mechanical equilibrium remains valid but reduces

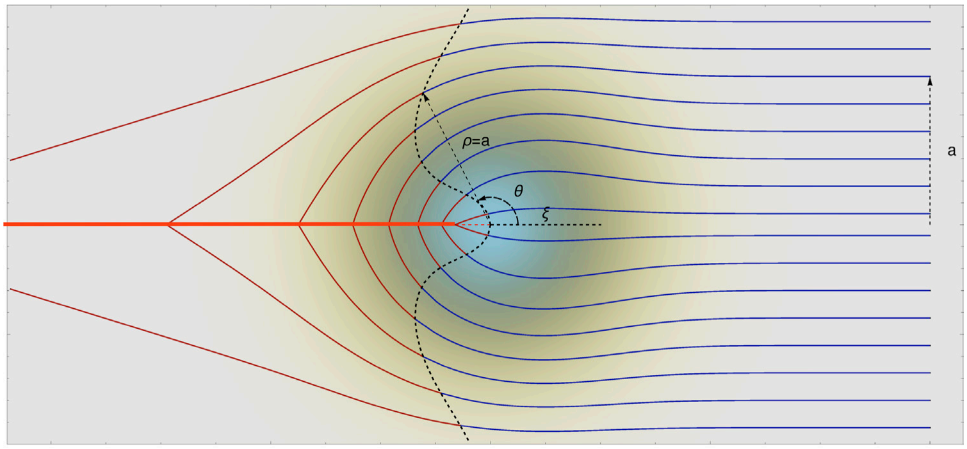

Figure 10. Characteristics (or rays) of the eikonal equation for a plane with a Gaussian bulge of size ξ. The smectic wave comes in from the right where the characteristics are parallel to the horizontal axis. Characteristics are indexed by their distance a from the horizontal axis at plus infinity. Near the bulge, the characteristics refract. The shortest distance of the characteristic to the center of the bulge equals a. At that point the 'minus' solution for the characteristics defined by equation (4.4*b*) must be matched to a 'plus' characteristic. The locus of points of nearest approach are indicated by a dashed line. Blue: minus characteristics. Red: plus characteristics. A *caustic* extends along the negative x-axis starting from the center of the bulge (heavy red line).

to the *local* relation $P = 2\gamma(\mathbf{s})H(\mathbf{s})$ where $\gamma(\mathbf{s})$ is the tension and where $H(\mathbf{s})$ is the curvature at location $\mathbf{s}$. If the tension variation is small, one can expand $\gamma(\mathbf{s}) = \gamma_0 + \delta\gamma(\mathbf{s})$ and $H(\mathbf{s}) = 1/R + \frac{1}{2}\Delta\zeta(\mathbf{s})$ with $\zeta(\mathbf{s})$ the radial outward displacement and with Δ the Laplace–Beltrami operator. Linearizing the Laplace Law gives

$$\gamma_0\Delta\zeta(\mathbf{s}) \simeq 2\delta\gamma(\mathbf{s})/R. \tag{4.1}$$

Equation (4.1) has the form of the Poisson equation with $2(\delta\gamma(\mathbf{s})/\gamma_0)/R$ playing the role of the effective 'charge density' . If there is a localized reduction in tension, then the resulting displacement is an outward bulge that decays logarithmically away from the region of the tension deficit. If the increased elastic strain of the surface in the center of the bulge causes additional weakening of the tension—through anharmonic elastic effects—then this can lead to catastrophic failure. Here, we will restrict ourselves to the question whether smectic order is able to suppress the initial bulge formation as described by equation (4.1) for the case of a uniform liquid.

The energy variation associated with bulge formation has the form

$$\delta E_l = \int \mathrm{d}a\left(\frac{1}{2}\gamma_0(\nabla\zeta)^2 + 2\delta\gamma(\zeta/R)\right). \tag{4.2}$$

Minimization of δE_l reproduces equation (4.1). In general, if the surface tension is reduced by an amount $\delta\gamma_0$ over a region of size ξ then $\delta E_l = c_1\gamma_0\zeta_0^2 - c_2|\delta\gamma|(\zeta_0/R)\xi^2$ with ζ_0 the height of the bulge, $\delta\gamma$ the mean reduction of the tension, and $c_{1,2}$ numerical constants of the order of one.

4.1. Eikonal solution

We now will solve the eikonal solution $|\nabla\phi|^2 = k_0^2$ for a bulge centered at the origin of a *flat* plane. Assume a localized vertical displacement ζ of the surface that depends only on the distance ρ from the origin. The eikonal equation in polar coordinates is:

$$(1+\zeta_\rho^2)^{-1}\phi_\rho^2 + \rho^{-2}\phi_\theta^2 - k_0^2 = 0. \tag{4.3}$$

This first-order differential equation can be solved using the method of characteristics. The result is

$$\frac{\mathrm{d}\phi^\pm}{\mathrm{d}\rho} = \pm k_0\frac{\sqrt{(1+\zeta_\rho^2)(\rho^2-a^2)}}{\rho} \tag{4.4a}$$

$$\frac{\mathrm{d}\theta^\pm}{\mathrm{d}\rho} = \pm a\frac{\sqrt{(1+\zeta_\rho^2)}}{\rho\sqrt{\rho^2-a^2}}. \tag{4.4b}$$

Here, $\theta(\rho)$ is the polar angle measured from the origin and a a free parameter. For given a, this pair of equations defines a characteristic curve in the $x-y$ plane that is a 'flow-line' of the director field of the smectic. For given polar angle θ, the distance of the characteristic from the origin must be obtained by inverting $\theta(\rho)$. The characteristics for a bulge with a Gaussian shape are shown in figure 10. For large positive x, where the smectic is undeformed, the characteristics are lines parallel to the x axis. When they approach the bulge they bend towards the x-axis, somewhat like the rays of a wave front diffracted by a lens. For negative x, the characteristics are again straight lines but rotated with respect to the 'incident' wave. The parameter a is the distance of closest approach of a characteristic to the origin. The 'minus' solution of equation (4.4*b*) will apply to the characteristics of the incoming wave and the plus solution to the characteristics of the refracted wave. The plus and minus solutions for a characteristic must be matched at the point where $\rho = a$. The locus of matching points for different characteristic is indicated by a dashed line in figure 10. The refracted characteristics coming from opposite sides of the bulge intersect along the negative x-axis. In the language of geometric optics, the locus of intersection points of

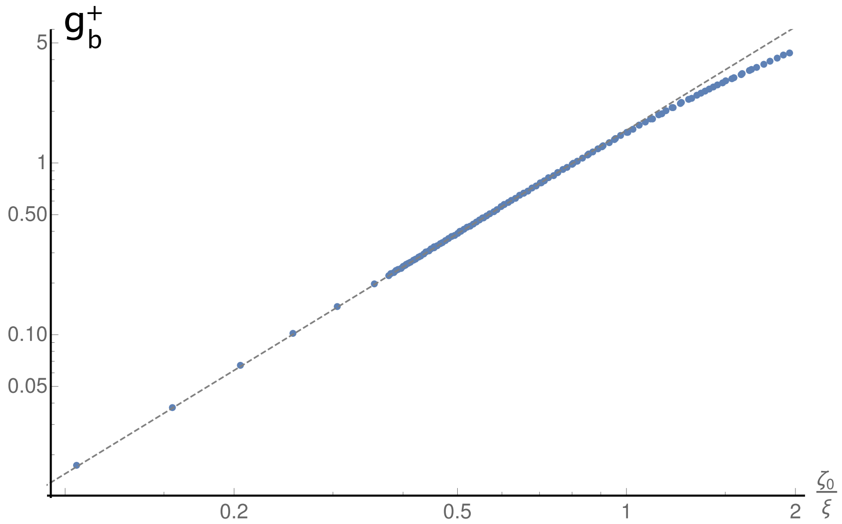

Figure 11. Scaling function $g_b^+(x)$ for the plus solution as a function of the ratio of the bulge height ζ_0 and the bulge width ξ on a log–log scale. The straight line has a slope 2.0.

characteristics are known as a *caustic* (shown as a heavy red line in figure 10).

Explicit expressions for the characteristics can be obtained by perturbing around the uniform state. In perturbation theory, a characteristic with parameter a can be shown to terminate along the caustic at the point $x = -\varrho(a)$ defined by

$$\frac{a^2}{\xi^2} = \ln\left(\frac{\zeta_0^2\sqrt{\pi}\varrho(a)}{2\xi^3\left(1+\frac{\zeta_0^2}{4\xi^2}\mathrm{e}^{-\varrho(a)^2/\xi^2}\right)}\right). \tag{4.5}$$

For $\varrho(a)$ large compared to ξ, this can be appoximated by

$$\frac{a^2}{\xi^2} \simeq \ln\left(\frac{\sqrt{\pi}\zeta_0^2\varrho(a)}{2\xi^3}\right). \tag{4.6}$$

Note that $\varrho(a)$ has a lower bound $\varrho(a=0)$ defined by the condition that the argument of the logarithm equals one. This is the case if $\varrho(a=0) = \frac{2\xi^3}{\sqrt{\pi}\zeta_0^2}$.

4.2. Bulge bending energy

For a given solution of the eikonal equation, the bending energy of the bulge has the form $F_b = \frac{1}{2}A_0^2\int \mathrm{d}a\Delta\phi^2 = \frac{1}{2}K\int \mathrm{d}a\,[\nabla\cdot\hat{\mathbf{n}}_e]^2$. In terms of the characteristics, the bending energy can be expressed as the sum of plus and minus terms:

$$\frac{1}{2}A^2\Bigg(\underbrace{\int_{-\infty}^{\infty}\mathrm{d}a\int_{\infty}^{a}\mathrm{d}\rho(\Delta\phi^-)^2\rho\sqrt{1+\zeta_\rho^2}|\theta_a|}_{\text{plus}}$$
$$+\underbrace{\int_{-\infty}^{\infty}\mathrm{d}a\int_{a}^{\varrho(a)}\mathrm{d}\rho(\Delta\phi^+)^2\rho\sqrt{1+\zeta_\rho^2}|\theta_a|}_{\text{minus}}\Bigg) \tag{4.7}$$

where $\varrho(a)$ must be found from the solution of the equation

$$\theta^+(\varrho, a) = \pi. \tag{4.8}$$

We evaluated the bending energy for the case of a Gaussian bulge $\zeta(\rho) = \zeta_0\mathrm{e}^{-\rho^2/(2\xi^2)}$. The bending energy has the general form $F_b/K = g_b^+(\zeta_0/\xi) + g_b^-(\zeta_0/\xi)$ with $g_b^{\pm}(x)$ separate dimensionless scaling functions for the plus and minus solutions. The (numerically computed) scaling function $g_b^+(x)$ for the plus solution is shown in figure 11. The figure shows that $g_b^+(x) \propto x^2$ for small $x = \zeta_0/\xi$. Explicitly, the plus bending energy has the form

$$F_b(+) \simeq 1.55K(\zeta_0/\xi)^2. \tag{4.9}$$

In the same manner, the minus bending energy is found to have the form

$$F_b(-) \simeq 0.035K(\zeta_0/\xi)^4. \tag{4.10}$$

The minus bending is always small compared to the plus bending energy.

To understand these results, one can use again perturbation theory. Assume that the phase degree of freedom has the form $\phi(x, y) = \mathbf{k}\cdot(x, y) + k_0u(x, y)$, with $u(x, y)$ the displacement of the stripes along the wavevector direction and with $\mathbf{k} = \hat{\mathbf{n}}k_0$ where $\hat{\mathbf{n}}$ is a unit vector along the direction of the unperturbed plane wave. Expanding the LB free energy to lowest order in both $\zeta(x, y)$ and $u(x, y)$ gives

$$F_{\mathrm{LB}} \simeq \frac{1}{2}\int\Big\{B\Big[\hat{\mathbf{n}}\cdot\nabla u - \frac{1}{2}(\hat{\mathbf{n}}\cdot\nabla\zeta)^2\Big]^2$$
$$+K\Big[\Delta u - \hat{\mathbf{n}}^T\mathbf{C}\nabla\zeta\Big]^2\Big\}\,\mathrm{d}x\mathrm{d}y + ... \tag{4.11}$$

Here,

$$\mathbf{C} = \begin{pmatrix}\zeta_{yy} & -\zeta_{xy}\\ -\zeta_{xy} & \zeta_{xx}\end{pmatrix} \tag{4.12}$$

is the curvature tensor of the surface. Demand that $u(x, y)$ is a solution of the eikonal solution, which means setting the first term of F_{LB} to zero so $\hat{\mathbf{n}}\cdot\nabla u = \frac{1}{2}(\hat{\mathbf{n}}\cdot\nabla\zeta)^2$. Power counting shows that for a bulge $\zeta(\rho) = \zeta_0\mathrm{e}^{-\rho^2/(2\xi^2)}$ the displacement scales as $u \sim \zeta_0^2/\xi$ since ξ is the only lateral length scale of the

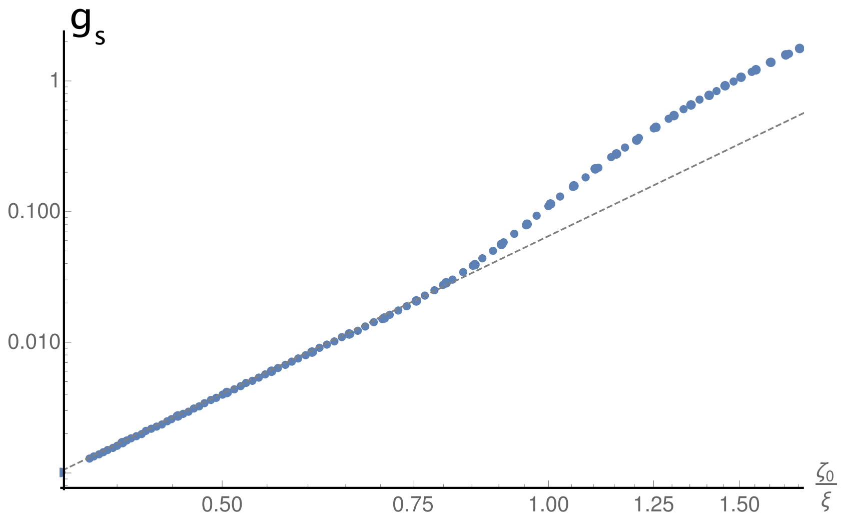

Figure 12. Suture energy for the caustic on a log–log scale. Vertical axis: Dimensionless suture energy g_s equal to $F_s/(Kk_0\xi)$. Horizontal axis: ratio of the bulge height ζ_0 and the bulge width ξ. Straight line $0.65(\zeta/\xi)^4$.

problem that can appear in derivatives. Insert this estimate in the bending energy area density $K\left[\Delta u - \hat{\mathbf{n}}^T\mathbf{C}\nabla\zeta\right]^2$. If the first term inside the square brackets dominates, then the bending energy should be of the order of $K\xi^2(\zeta^2/\xi^3)^2 \sim K\zeta^4/\xi^4$. If the second term dominates, then the bending energy should be of the order of $K\xi^2(\zeta/\xi^2)^2 \sim K\zeta^2/\xi^2$. These two limiting cases neatly correspond to the plus and minus regimes.

4.3. Suture energy

The two eikonal solutions that meet along the negative x-axis along a caustic must be stitched together into a single continuous solution. The two incoming wavevectors have the same projection k_x along the x direction but opposite projections $\pm k_y$ along the y-direction, with $k_x^2 + k_y^2 = k_0^2$ where $|k_x|$ approaches k_0 for large negative x.

In the region where the two solutions must be matched around $y = 0$, we look for solutions of the form

$$\phi(x, y) \simeq k_x x + f(y) \tag{4.13}$$

where f_y should equal $\pm k_y$ far from the x-axis. Inserting this ansatz in the constant amplitude expression for F_{LB} gives the following expression for the 'suture energy' F_s:

$$F_s \simeq A_0^2 \int\int \left(f_{yy}^2 + [k_y^2 - f_y^2]^2\right) \mathrm{d}x\,\mathrm{d}y \tag{4.14}$$

where $A = A_0 = \sqrt{-r/2u}$ as before. Define, $q \equiv f_y$. We need to minimize

$$F_s \simeq A_0^2 \int\int \left(q_y^2 + [k_y^2 - q^2]^2\right) \mathrm{d}x\,\mathrm{d}y \tag{4.15}$$

with respect to $q(y)$. The Euler–Lagrange equation

$$-q_{yy} + 2(q^2 - k_y^2)q = 0 \tag{4.16}$$

has the soliton-type solution

$$q(y) = k_y \tanh(k_y y) \tag{4.17}$$

which has the appropriate limiting behavior far from the x-axis. After integration over y, the singular energy reduces to

$$F_s \simeq (8/3)A_0^2 \int_0^{-\infty} |k_y|^3\,\mathrm{d}x. \tag{4.18}$$

For $|k_y(x)|$ we inserted the value $\partial\phi/\partial y|_{y=0}$ obtained from the eikonal solution. The result of the numerical evaluation of this integral is shown in figure 12: since ξ is the characteristic variation scale for the bulge, equation (4.18) suggests the scaling form $F_s = A_0^2(k_0^3\xi)g_s(\zeta_0/\xi)$. We found that if we plotted our results with $F_s/(Kk_0\xi)$ as the vertical axis and ζ_0/ξ as the horizontal axis then all our data indeed collapsed onto the single curve that is shown in figure 12. The scaling function $g_s(x)$ is, for small x proportional to x^4 with

$$F_s/(Kk_0\xi) \simeq 0.65(\zeta_0/\xi)^4.$$

The key result here is that the scaling function is of the order of one when x is of the order of one. The characteristic energy scale of the suture energy is thus $Kk_0\xi$. This must be compared with the characteristic energy scale K for the bending energy. For bulges with $k_0\xi$ large compared to one, the suture energy dominates over the bending energy.

4.4. Smectic capsids and bulge formation

We can now examine the formation of a Gaussian bulge on a smectic capsid. Add our earlier expression for the energy cost of the formation of a bulge on a liquid shell of width ξ to the sum of bending and suture energies:

$$\begin{aligned}\delta E_{\mathrm{B}} = {} & \gamma_0\zeta_0^2 - |\delta\gamma|(\zeta_0/R)\xi^2 + K(\zeta_0/\xi)^2 \\ & + K(k_0\xi)(\zeta_0/\xi)^4\end{aligned} \tag{4.19}$$

where $\delta\gamma$ is the typical reduction of the tension across the bulge. For clarity, we leave out the numerical prefactors. In the liquid state, where $K = 0$, the bulge height minimizing δE_{B} would be

$$\zeta^* \sim (|\delta\gamma|/\gamma_0)\xi^2/R.$$

The energy gain $-\gamma_0\zeta^{*2}$ by the formation of the bulge—due to work by the pressure difference γ_0/R—grows rapidly with the size ξ of the bulge. In order for the smectic order to suppress bulge formation, we must require that the bending and suture energy costs exceed the energy gain. This is the case if

$$\gamma_0\zeta^{*2} < K(\zeta^*/\xi)^2 + K(k_0\xi)(\zeta^*/\xi)^4. \qquad (4.20)$$

Because both the work by the pressure (i.e. the left-hand side) and the bending energy are proportional to ζ^{*2}, it follows that bending energy can suppress bulging if K is significantly larger than $\gamma_0\xi^2$. Because the suture energy has a different dependence on ζ^*, we will compare instead the work by the pressure and the suture energy for the case that $\zeta^* = \xi$. This is the point where the bulge could be expected to strain the capsid to the point that it weakens the local elastic response. The suture energy exceeds the pressure work if K is significantly larger than $\gamma_0\xi/k_0$. If the size ξ of the weakened section is large compared to the microscopic cutoff $1/k_0$ then the suture energy is much more effective in suppressing bulging than the bending energy.

Under what conditions would the suture energy be sufficiently large to suppress bulging? Let λ_p be the *persistence length* of the presumed capsid protein chains. The bending modulus K can be expressed in terms of this persistence length as $k_BT(k_0\lambda_p)$. Let P be the osmotic pressures of the archaeal virus. Then $\gamma_0 \simeq PR$. In terms of these quantities, the stability condition is that $k_BT(k_0\lambda_p)$ must exceed $PR\xi/k_0$. The maximum osmotic pressure that a smectic capsid could withstand is thus

$$P_{\max} \sim k_BTk_0^2\lambda_p/(R\xi).$$

Assume a capsid with a size in the range of 50–100 nanometers (nm) has a defected region with a size in the range of 10 nm. Next assume a filament peristence length λ_p in the range of one micron and assume a microscopic cutoff $1/k_0$—the size of a capsid protein—in the range of nanometer. For these values, the maximum pressure the smectic caspid could withstand would be in the range of 10 atmospheres. This is comparable to the osmotic pressure inside conventional phage viruses, which suggests that smectic capsids indeed could withstand significant osmotic pressures. Note that increasing the stiffness of the polymer chains in order to increase the maximum pressure would have the (undesired) effect of freezing the protein array. This is undesired because large shape changes would be inhibited. More definite estimates have to await measurement of the persistence length of the capsid protein chains of the archaeal viruses (if any). It certainly would be interesting if synthetic smectic capsids composed polymerizing chiral proteins could be fabricated in which case the persistence length would be known.

Acknowledgments

We would like to acknowledge important discussions with Alexander Grosberg and Randy Kamien as well as support from the NSF under DMR Grant 1309423.

ORCID iDs

R F Bruinsma https://orcid.org/0000-0002-7739-6002

References

[1] Gelbart W M and Knobler C M 2009 *Science* **323** 1682
[2] Roos W, Bruinsma R and Wuite G 2010 *Nat. Phys.* **6** 733
[3] Prangishvili D, Bamford D H, Forterre P, Iranzo J, Koonin E V and Krupovic M 2017 *Nat. Rev. Microbiol.* **15** 724–39
[4] Torchilin V 2012 *Adv. Drug Deliv. Rev.* **64** 302–15
[5] Caspar D L and Klug A 1962 *Cold Spring Harbor Symposia on Quantitative Biology* vol 27 (New York: Cold Spring Harbor Laboratory Press) pp 1–24
[6] Woese C R and Fox G E 1977 *Proc. Natl Acad. Sci.* **74** 5088
[7] Woese C R, Kandler O and Wheelis M L 1990 *Proc. Natl Acad. Sci.* **87** 4576
[8] Woese C R 2004 *Microbiol. Mol. Biol.* **68** 173
[9] Pina M, Bize A, Forterre P and Prangishvili D 2011 *FEMS Microbiol. Rev.* **35** 1035
[10] Häring M, Peng X, Brügger K, Rachel R, Stetter K O, Garrett R A and Prangishvili D 2004 *Virology* **323** 233
[11] Lawrence C M, Menon S, Eilers B J, Bothner B, Khayat R, Douglas T and Young M J 2009 *J. Biol. Chem.* **284** 12599
[12] Hochstein R, Bollschweiler D, Engelhardt H, Lawrence C M and Young M 2015 *J. Virol.* **89** 9146
[13] Perotti L, Dharmavaram S, Klug W, Marian J, Rudnick J and Bruinsma R 2016 *Phys. Rev.* E **94** 012404
[14] Prangishvili D, Vestergaard G, Häring M, Aramayo R, Basta T, Rachel R and Garrett R 2006 *J. Mol. Biol.* **359** 1203
[15] Häring M, Vestergaard G, Rachel R, Chen L, Garrett R A and Prangishvili D 2005 *Nature* **436** 1101
[16] Irvine W, Vitelli V and Chaikin P 2010 *Nature* **468** 947
[17] Bruinsma R, Halperin B and Zippelius A 1982 *Phys. Rev.* B **25** 579
[18] Mogilner A and Oster G 2003 *Biophys. J.* **84** 1591
[19] Derényi I, Jülicher F and Prost J 2002 *Phys. Rev. Lett.* **88** 238101
[20] Hochstein R, Bollschweiler D, Dharmavaram S, Lintner N G, Plitzko J M, Bruinsma R, Engelhardt H, Young M J, Klug W S and Lawrence C M 2018 *Proc. Natl Acad. Sci.* **115** 2120
[21] Delaunay C 1841 *J. Math. Pures Appl.* **6** 309
[22] Hanhijärvi K, Ziedaite G, Pietilä M, Hæggström E and Bamford D 2013 *Biophys. J.* **104** 2264
[23] Grinstein G and Pelcovits R A 1981 *Phys. Rev. Lett.* **47** 856
[24] Kamien R D, Nelson D R, Santangelo C D and Vitelli V 2009 *Phys. Rev.* E **80** 051703
[25] Matsumoto S, Kawamoto M and Kaneko N 1975 *Appl. Phys. Lett.* **27** 268
[26] Helfrich W and Prost J 1988 *Phys. Rev.* A **38** 3065